ACS APPLIED MATERIALS & INTERFACES

Research Article

www.acsami.org

Oxygen Vacancy Enhanced Photocatalytic Activity of Pervoskite $SrTiO_3$

Huaqiao Tan,[†] Zhao Zhao,[†,‡] Wan-bin Zhu,[§] Eric N. Coker,[∥] Binsong Li,[∥] Min Zheng,[†] Weixing Yu,[§] Hongyou Fan,[∥,⊥] and Zaicheng Sun*[,†]

[†]State Key Laboratory of Luminescence and Applications, Changchun Institute of Optics, Fine Mechanics and Physics, Chinese Academy of Sciences, 3888 East Nanhu Road, Changchun 130033, P. R. China

[‡]University of Chinese Academy of Sciences, Beijing 100000, P. R. China

[§]State Key Laboratory of Applied Optics, Changchun Institute of Optics, Fine Mechanics and Physics, Chinese Academy of Sciences, Changchun 130033, P. R. China

[∥]Advanced Materials Laboratory, Sandia National Laboratories, P.O. Box 5800 MS1349, Albuquerque New Mexico 87185-1349, United States

[⊥]Center for Micro-Engineering and Materials, Department of Chemical and Nuclear Engineering, University of New Mexico, Albuquerque, New Mexico 87106, United States

Supporting Information

ABSTRACT: A facile and general method has been developed to fabricate oxygen vacancies on perovskite $SrTiO_3$ (STO) nanocrystals through a controllable solid-state reaction of $NaBH_4$ and $SrTiO_3$ nanocrystals. STO samples with tunable color, oxygen vacancy concentration on nanocrystal surface have been synthesized. TEM results reveal that these STO samples have a crystalline core/amorphous shell structure ($SrTiO_3$@$SrTiO_{3-x}$). XPS and EPR results disclose that the oxygen vacancy concentration increases with the increase of reaction time and temperature. The concentration of oxygen vacancies calculated from TGA data, could reach 5.07% (atom) in this study. UV−vis spectra and photocatalytic results indicate that oxygen vacancies on STO surface play an important role in influencing the light absorption and photocatalytic performance. However, an excess amount of oxygen vacancies leads to a decrease of photocatalytic performance. The optimal photocatalytic activity for H_2 production under UV−vis irradiation is up to 2.2 mmol h^{-1} g^{-1}, which is about 2.3 times than the original $SrTiO_3$, corresponding to 3.28% (atom) of oxygen vacancy concentration.

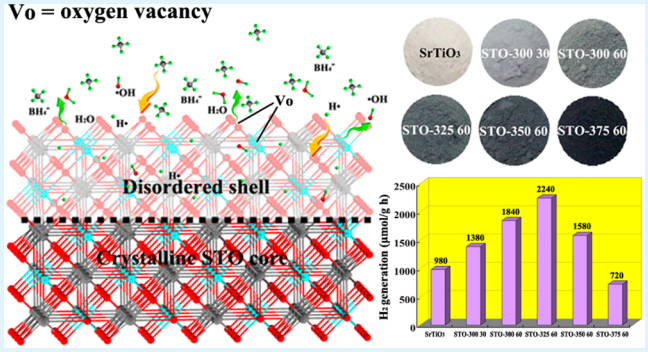

KEYWORDS: *$SrTiO_3$, $NaBH_4$, oxygen vacancy, core/shell nanostructure, photocatlytic H_2 generation*

INTRODUCTION

Photocatalysis, as an efficient, green, and promising solution to the current energy crisis and environmental deterioration, has attracted considerable interest.[1−6] Among various semiconductors, perovskite metal oxides such as $SrTiO_3$ are promising photocatalysts because of their exceptional electronic and optical properties, photochemical stability, low cost, and high catalytic efficiency.[7] However, the wide band gap of $SrTiO_3$ (3.2 eV) makes it active only under UV light irradiation. Thus, many works have been devoted to expand the spectral response of $SrTiO_3$, such as doping with metals,[8,9] and nonmetals,[10,11] and combining with another semiconductor.[12] Furthermore, the high electron−hole recombination rate of $SrTiO_3$ results in low photocatalytic efficiency. Therefore, to date, it is still a challenge to enhance the photocatalytic efficiency of $SrTiO_3$. One of the most efficient way to improve the photocatalytic performance is by reducing the electron−hole recombination.[13]

As well-known, oxygen defect plays an important role in the processes of photocatalysis.[14] Surface oxygen vacancies can act as the photoinduced charge traps and the adsorption sites, in which the charge can transfer to the adsorbed compounds, thus prevent the recombination of photogenerated charge carriers, resulting in the improvement of the photocatalytic performance; while the bulk oxygen vacancies only serve as charge carrier traps where the photogenerated electron−hole recombine, which leads to the decrease of photocatalytic performance.[15,16] Therefore, controlling the oxygen defects on the surface of photocatalyst could be very important for the improvement of its photocatalytic property. Recently, Mao and co-workers reported a breakthrough method to generate a

Received: August 4, 2014
Accepted: October 13, 2014
Published: October 13, 2014

disorder layer in the TiO_2 surface by hydrogenation, which caused substantial solar-driven photocatalytic performances.[17] Then, some similar results that surface oxygen defects promote the photocatalytic activity have been successively reported by Li, Huang, and Zhu, involving TiO_2,[18−23] WO_3,[24] ZnO,[25,26] and Fe_2O_3.[27] Very recently, Rappe et al. also demonstrated that a perovskite solid solution $[KNbO_3]_{1-x}[BaNi_{1/2}Nb_{1/2}O_{3-\delta}]_x$ (KBNNO) with a certain oxygen vacancy has a narrow band gap and has potential to be a solar energy conversion material.[28] In a word, perovskite metal oxides with oxygen vacancies have seldom been investigated, especially the relationship between oxygen vacancy concentration and photocatalytic performance.

Herein, a facile and general method is introduced to fabricate oxygen vacancies on $SrTiO_3$ nanocrystal surfaces through a controllable solid-state reaction of $NaBH_4$ and crystalline $SrTiO_3$. A series of colored $SrTiO_3$ from white via gray, blue, and, finally, to black have been synthesized. TEM results reveal that these colored $SrTiO_3$ have a crystalline core/amorphous shell structure ($SrTiO_3$@$SrTiO_{3-x}$). XPS, EPR, and TGA results showed the oxygen vacancy concentration increases as the color of the material darkened and reaches a maximum of 5.07% (atom). The photocatalytic H_2 production activity shows an increase and then decrease trend with the increase of oxygen vacancy concentration. Among these samples, the optimal photocatalytic activity for H_2 production under UV−vis irradiation is up to 2.2 mmol h^{-1} g^{-1}, which is about 2.3 times than the original $SrTiO_3$, corresponding to the concentration of oxygen vacancy of 3.28% (atom).

EXPERIMENTAL SECTION

Chemicals and Materials. $Sr(OH)_2{\cdot}8H_2O$ (99.5%), NaOH (96%), ethanol (AR), and $NaBH_4$ (98%) were purchased from Aladdin Reagent Company and used without any further purification. P25 TiO_2 was purchased from Degussa AG, Germany.

Preparation of $SrTiO_3$ Nanoparticles. 10.0 g (125 mmol) of P25 was added to 350 mL of 10 M NaOH solution, and then, the mixture was transferred into 500 mL Teflon-lined autoclave at 180 °C for 48 h. Then, a solid sample was isolated by filtering. The sample was washed with 0.1 M HCl solution and distilled water until the pH value of the rinsing solution reached about 6.5. As-prepared titanic hydroxide (0.8 g) and 8.0 g (30 mmol) of $Sr(OH)_2{\cdot}8H_2O$ were dispersed in 40 mL distilled water. Subsequently, the mixture was transferred to 50 mL Teflon-lined autoclaves by hydrothermal treatment at 180 °C for 12 h. The white powder was centrifuged, washed with diluted acetic acid, deionized water for several times, and dried at 70 °C.

Preparation of Colored $SrTiO_3$@$SrTiO_{3-x}$. 4.5880 g (25 mmol) of as-prepared $SrTiO_3$ powder and 0.9510 g (25 mmol) of $NaBH_4$ were mixed in an agate mortar and ground for 30 min. Then, the mixture was put in a porcelain boat, placed in a tubular furnace, heated from room temperature to 300−375 °C under Ar atmosphere at a heating rate of 10 °C min^{-1}, and then held at the designed temperature for about 30−60 min. After naturally cooling, the colored STO sample was obtained by simply washing with deionized water and ethanol for several times to remove the unreacted $NaBH_4$ and dried at 70 °C. A series of colored STO samples tuned from light gray to black can be obtained by controlling the reaction time and temperature. The resulting samples were denoted as STO-*T t*, where *T* and *t* are the reaction temperature (*T* = 300, 325, 350, 375 °C) and time (*t* = 30, 60 min), respectively.

Characterization. X-ray diffraction (XRD) was performed on a Bruker AXS D8 Focus X-ray diffractometer (XRD) with a Cu Kα radiation (λ = 1.54056 Å). The UV−vis spectra were measured on a Shimadzu UV 2600 UV/vis spectrophotometer. Scanning electron microscope (SEM) images were taken on a JEOL JSM 4800F. Transmission electron microscope (TEM) images were obtained on an FEI Tecnai G2 operated at 200 kV. X-ray photoelectron spectra (XPS) were collected by using an ESCALABMKII spectrometer with an Al Kα (1486.6 eV) achromatic X-ray source. The EPR spectra were recorded on a Bruker EMX-8 spectrometer operated at 9.44 GHz 300 K.

Thermogravimetric analysis (TGA) was recorded on an STA 449 F3 Jupiter (Netzsch Instruments, Selb, Germany) coupled to a Mass Spectrometer (MS, Hiden Analytical, model HPR-20). Specimens were placed in Pt crucibles, and TGA-MS data were recorded during heating from ambient temperature to 800 °C under flowing air (90 mL min^{-1}) mixed with argon (10 mL min^{-1}). A heating rate of 10 °C min^{-1} was used for all experiments, and background correction was applied by subtracting data for a blank run (without specimen) from each experiment. To generate differential-TGA plots, the TGA data for pristine $SrTiO_3$ was subtracted from the TGA data of STO-*T t* samples, thus accentuating the difference between the treated and untreated $SrTiO_3$ materials. An arbitrary mass offset was applied in plotting the data so that the data coincided at 200 °C to simply interpretation of mass increases during oxidation above 200 °C.

Photocatalytic H_2 Generation. 50 mg of samples with 1.0 wt % Pt loaded was dispersed in 120 mL 25% aqueous methanol solution in a closed Perfect Light Company Labsolar-III (AG) gas circulation system. Methanol was acted as a sacrificial reagent. The amount of H_2 production was determined by using an online Schimazu GC-2014c gas chromatography.

Photoelectrode Preparation. According to the procedure in refs 29 and 30, electrophoretic deposition was used to deposited the STO samples on a FTO transparent conductive glass substrate, as shown following: 40 mg of STO sample was dispersed in a 50 mL of 0.2 mg/mL I_2/acetone solution under ultrasonic treatment. A two-electrode process was used to deposit the samples at the applied potential of 20 V for 10 min. FTO glass substrates with the coated area about 1 × 3 cm^2 was used for both electrodes. Then, the deposited electrode was dried at 200 °C for 30 min to remove I_2 residues.

Photoelectrochemical Measurements. A conventional three-electrode process was used to investigate the photoelectrochemical properties of samples in a quartz cell. A FTO photoanode deposited STO samples, Hg/Hg_2Cl_2, and Pt foil electrode acted as the working electrode, reference electrode, and counter electrode, respectively. A 1.0 M NaOH aqueous solution was used as the electrolyte. The photoanode was illuminated by a Beijing Trusttech Co. Ltd., PLS-SXE-S500 300 W Xe lamp. The illuminated area was about 1 × 1 cm^2. The IPCE (incident photon-to-current conversion efficiency) was calculated as the following equation:

$$\mathrm{IPCE}\ (\%) = \frac{1240 \times \text{photocurrent density (mA cm}^{-2})}{\text{wavelength (nm)} \times \text{photon flux (mW cm}^{-2})} \times 100$$

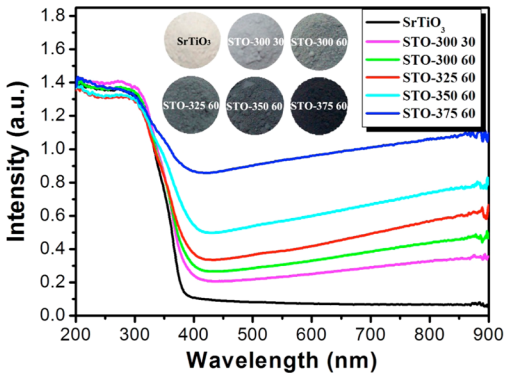

Figure 1. UV−vis diffuse reflectance spectra of pristine $SrTiO_3$ and STO samples; the insets are photographs of pristine $SrTiO_3$ and STO samples.

RESULTS AND DISCUSSION

Structure Features and Physical Properties. In the method, $NaBH_4$ acts as an oxygen scavenger,[31] which decomposed and in situ produced the active hydrogen at mild reaction temperature. This active hydrogen is more reactive than H_2 and other reductants in the previous reports.[17−26] Its strong reducing capability is beneficial to remove the oxygen atoms from the surface of $SrTiO_3$, thus forming oxygen vacancies at a relatively short time and low temperature, which is helpful to maintain the original morphology of $SrTiO_3$ nanocrystals. By tuning the reaction time and temperature, the oxygen vacancy concentration can be tailored easily. Thus, a series of colored $SrTiO_3$ with different photocatalytic activities were obtained. In addition, the byproducts from $NaBH_4$ can be removed easily by washing with water and ethanol. The XPS results indicate that there is no B or Na remaining in the washed and dried samples (Supporting Information Figure S1).

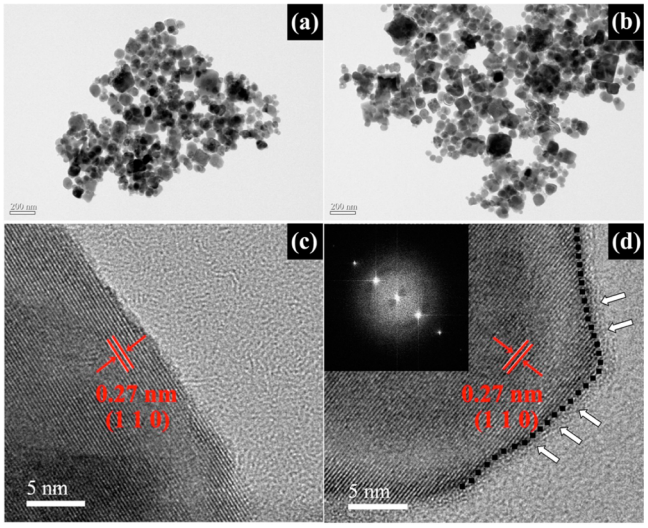

Figure 2. TEM images of pristine $SrTiO_3$ (a) and STO-325 60 (b); (c−d) HRTEM images of pristine $SrTiO_3$ nanocrystals (c), STO-325 60 (d). The dash line in part d displays the boundary of crystalline and disordered layer, the white arrows point to the disordered layer.

UV−vis diffuse reflectance spectra (Figure 1) show that pristine $SrTiO_3$ and STO-*T t* exhibit the absorption onset at 390 nm, which agrees with the band gap edge absorption of $SrTiO_3$ (3.2 eV). In contrast to pristine $SrTiO_3$, an additional absorption band beyond 400 nm extending to the infrared region is observed for STO-*T t* samples. The absorption band increases with the increase of reaction time and temperature, which agrees with the color change of samples. As shown in Figure 1, the color of $SrTiO_3$ turned from white to light gray and finally into black. It is generally accepted that the variable light absorption of $SrTiO_3$ is caused by the increasing oxygen vacancy concentration on $SrTiO_3$ surface.[23] With the increasing of oxygen vacancies, some reduced Ti sites such as Ti^{3+} could be formed, which is attributed to the light absorption beyond 400. In addition, these STO-*T t* samples show high stability and almost negligible change at ambient conditions over a year (Supporting Information Figure S2).

As shown in Figure 2, TEM images reveal that the particle size and morphology of STO samples before and after $NaBH_4$

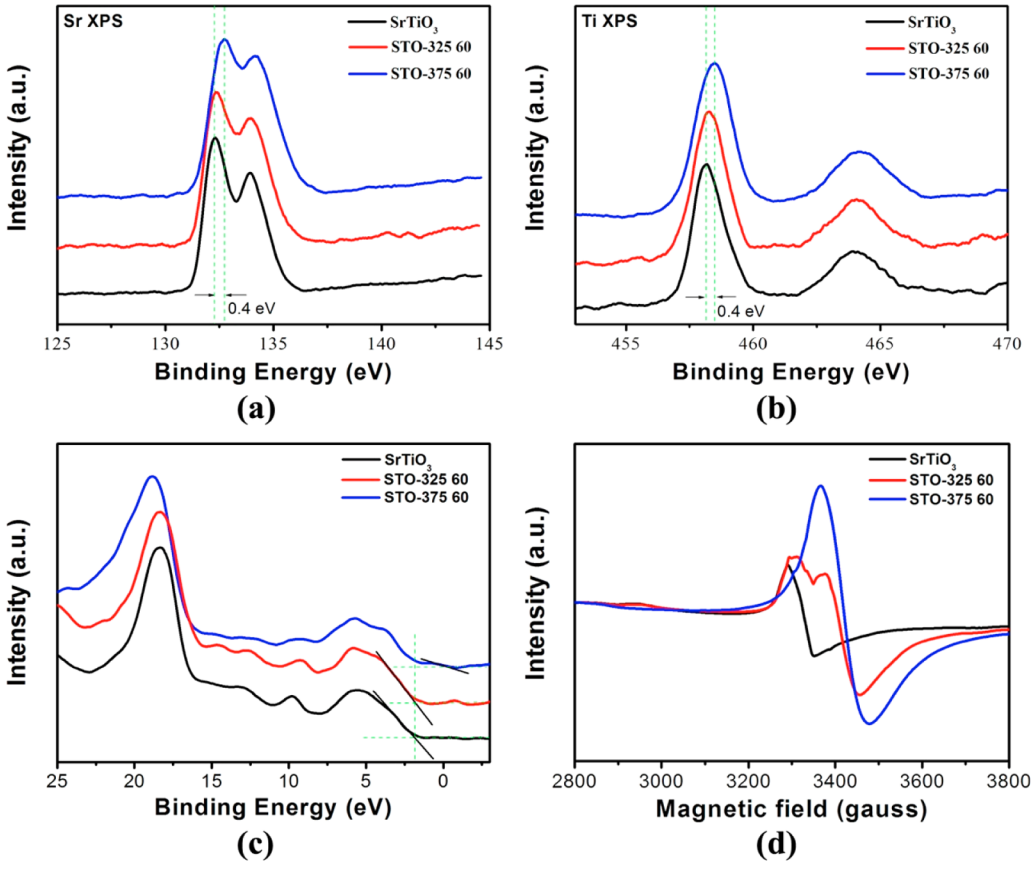

Figure 3. (a) Sr XPS spectra, (b) Ti XPS spectra, (c) XPS valence band spectra, and (d) EPR spectra of pristine $SrTiO_3$ and STO samples.

dx.doi.org/10.1021/am5051907 | ACS Appl. Mater. Interfaces 2014, 6, 19184−19190

treatment show no change. The average diameter of $SrTiO_3$ nanocrystals is ~50 nm. High-resolution TEM (HR TEM) images provide detailed information on the structure of $SrTiO_3$ nanocrystals. Before the reduction treatment, $SrTiO_3$ nanocrystals exhibit highly crystalline nature and well-resolved lattice feature throughout the whole particles (Figure 2c). When the treatment temperature rises up to 325 °C for 60 min, a disordered layer with ~1.2 nm thickness is clearly observed in the HR TEM images (Figure 2d). However, the core of nanocrystals is still highly crystalline. The lattice plane distances of crystalline core are 0.27 nm, which is the same as the lattice plane [1 1 0] of cubic $SrTiO_3$.[32,33] The HR TEM results confirm that all these STO samples have $SrTiO_3$@ $SrTiO_{3-x}$ core/shell structure feature.

XRD (X-ray diffraction) is used to characterize the change of crystalline phase of STO samples. Supporting Information Figure S3 shows the XRD patterns of pristine $SrTiO_3$ and STO-*T t*. The XRD patterns of STO-*T t* are quite similar to that of pristine cubic $SrTiO_3$ (JCPDS Card No. 035-0734).[34] The strong diffraction peaks indicate that STO-*T t* samples are highly crystalline as pristine $SrTiO_3$. However, a slightly broadening main peak is observed with increasing reaction time and temperature, which might be related to oxygen vacancies, as a result of lattice strains and the reduced crystallite size.[23]

XPS (X-ray photoelectron spectroscopy) is a powerful technology to investigate the chemical binding and valence band position of samples. The high-resolution spectra of Sr 3d, Ti 2p, O 1s XPS and valence band of pristine $SrTiO_3$ and STO-*T t* samples are shown in Figure 3 and Supporting Information Figure S4. After $NaBH_4$ treatment, it is found that with respect to the spectra of pristine $SrTiO_3$, the peaks of Sr, Ti and O shift to high binding energy gradually with the increasing reaction time and temperature. STO-375 60 shows the largest shift that is about 0.4 eV. This whole XPS shift is a characteristic shift of Fermi level.[35] The oxygen vacancy and reduced of $SrTiO_3$ surface aggrandize the equilibrium electron density, and thus push the Fermi level upward. The increased binding energies were observed. The VB XPS of STO samples are shown in Figure 3c. The pristine $SrTiO_3$ displayed the VB band edge at ~1.84 eV below the Fermi level. Because optical absorption spectra reveal that the band gap of $SrTiO_3$ is 3.20 eV, the conduction band minimum would be located at about −1.36 eV. The valence band maximum energy shows negligible change for the sample of STO-325 60. In the case of STO-375 60 sample, a blue-shift with the band tail about −0.15 eV has been observed, which may attribute to the phase change of reduced $SrTiO_3$.[23]

The O 1s high resolution XPS spectra of STO-*T t* can be fitted into three Gaussian peaks at 530.0 eV, 531.9 and 533.4 eV, respectively. The O 1s peak at 533.4 eV is usually assigned to the loosely bound oxygen on STO surface.[26] The component at 530.0 eV is associated with the O^{2-} ions in the crystal structure of STO.[36] And the middle peak at 531.9 eV, is attributed to O^{2-} in the oxygen defect of STO surface.[36,37] According to the previous report,[26] the intensity of middle peak is related to the concentration of oxygen vacancies on STO surface. As shown in Supporting Information Figure S4, the peak at 531.9 eV in STO samples turns stronger and stronger, indicating that the oxygen vacancy concentration on STO surface increases as the process of $NaBH_4$ treatment. Furthermore, EPR (electron paramagnetic resonance) spectra of STO samples were measured. As shown in Figure 3d, the pristine $SrTiO_3$ shows a sharp signal at g-value of ~2.01, which could be assigned to the Fe impurity of the synthesized STO.[35] The EPR signal observed in STO-*T t* with g = 1.97 can be assigned to paramagnetic oxygen vacancies, as documented in previous reference (e.g., Ta_2O_5, CeO_2, ZnO, etc.).[38] The signal intensity increases from STO 325 60 to STO 375 60, indicating that the oxygen vacancy concentration in STO-*T t* samples increases with the reaction process.

In order further to investigate the concentration change of oxygen vacancy in STO samples, the TGA in flowing Air/Ar mixture gas were measured. As shown in Figure 4, pristine

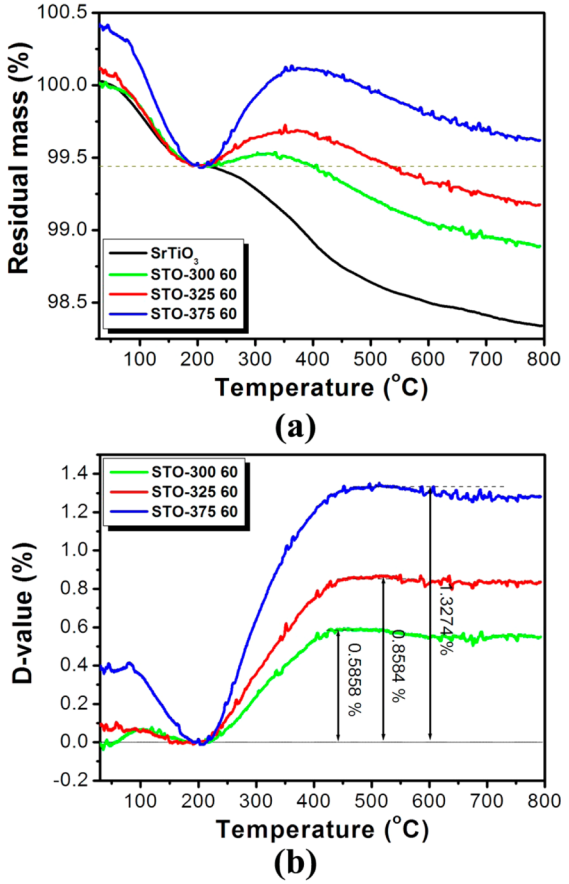

Figure 4. (a) TGA curve of pristine $SrTiO_3$ and STO-*T t* samples; (b) The TGA differential spectra of STO-*T t* samples with pristine $SrTiO_3$.

$SrTiO_3$ shows two weight loss stages in the temperature range 30−800 °C. As a result of mass spectra (Supporting Information Figure S5 and Figure S6) that monitored the gas coming out from samples during TGA measurement, water is the main weight loss. So the first weight loss can be assigned to the loss of physical adsorption water molecules on the STO surface. The second can be attributed to the loss of chemisorption waters and the escape of oxygen atoms on the STO surface under high temperature. In the cases of STO-*T t* samples, TGA curves display a weight loss first in temperature 30−210 °C, and a weight gain in 210−500 °C and then weight loss after 500 °C. As discussed above, the first weight loss can be assigned to the loss of surface and oxygen vacancy physical adsorption water molecules on the STO samples. After releasing the physical adsorbed water, the oxygen vacancies are ready to be refilled with oxygen in high temperature, causing a weight gain of STO-*T t* samples. After the oxygen

dx.doi.org/10.1021/am5051907 | ACS Appl. Mater. Interfaces 2014, 6, 19184−19190

vacancies are refilled, another weight loss similar as pristine $SrTiO_3$ has been observed. TGA differential spectra of STO-*T t* samples with pristine $SrTiO_3$ are shown in Figure 4b. After 210 °C, a positive D-value has been displayed, corresponding to the weight gain in TGA curves of STO samples. Then, D-value tends to a constant, which further indicate that the STO samples have similar weight loss as pristine $SrTiO_3$ after 500 °C. The D-value directly related to the refilled oxygen amount, which means the oxygen vacancy concentration. The D-value of STO-300 60, STO-325 60, and STO-375 60 with pristine $SrTiO_3$ are 0.5858%, 0.8584% and 1.3274%, respectively, corresponding to the oxygen vacancy concentration in STO-300 60, STO-325 60, and STO-375 60 are 2.24%, 3.28%, and 5.07% (atom), respectively.

Photocatalytic Activity and Photocurrent Response. The H_2 production from water under UV−vis irradiations was applied to evaluate the photocatalytic performance of STO samples. 50 mg samples with 1.0 wt % Pt loaded was dispersed in 120 mL 25% aqueous methanol solution. The UV−visible light source was a 300 W Xe lamp. As shown in Figure 5a, the steadily H_2 production is about 49 μmol h^{-1} for 0.05 g pristine $SrTiO_3$ (0.98 mmol h^{-1} g^{-1}). After it was treated by $NaBH_4$, the H_2 production rate of STO-*T t* was increased. For the gray STO-325 60, the maximum H_2 production was up to 112 μmol h^{-1} for 0.05 g STO-325 60 (2.2 mmol h^{-1} g^{-1}) under UV−visible light irradiations, which is 2.3 times than that of pristine $SrTiO_3$. The recycle experiments reveal that STO-325 60 shows negligible reduction of photocatalytic performance for H_2 generation after five recycles (Figure 5b), which indicated STO-325 60 has a good stability. The STO-*T t* samples obtained at higher reaction temperature or longer reaction time such as STO-350 60 and STO-375 60, the rates of H_2 production under UV−visible light are reduced to 79 and 36 μmol h^{-1} for 0.05 g sample (1.58 and 0.72 mmol h^{-1} g^{-1}), respectively, which might be related to the increase of oxygen defects in STO samples. It is well-known that the oxygen defects can act as an electron donors[39] and have a contribution to enhance the donor density of semiconductor.[20] With the increase of donor density, the charge transport in $SrTiO_3$ (Figure 5c) could be improved. The Fermi level of $SrTiO_3$ could also be shifted toward the conduction band.[40] This shift of the Fermi level can improve the charge separation at the STO/electrolyte interface. Therefore, the reasons for the enhanced photocatalytic activity in STO-325 60 could be mainly attributed to the enhancement of charge separation. However, when the oxygen vacancy concentration is too high, the defect can serve as a charge recombination center, and lower the free carrier mobility.[41] That results in a negative effect on the photocatalytic activities,[41] which could be the reason why the photocatalytic performances in STO-350 60 and STO-375 60 are reduced. In summary, at an optimum concentration, oxygen vacancy can improve the separation of photoexcited charge carriers. While beyond the optimum point, the photocatalytic performance would decrease. In our cases, the optimum concentration of oxygen vacancy is approximate 3.28% (atom) on the base of the TGA results.

In order to verify the improvement in charge separation of the photogenerated charge carriers for STO-325 60, the

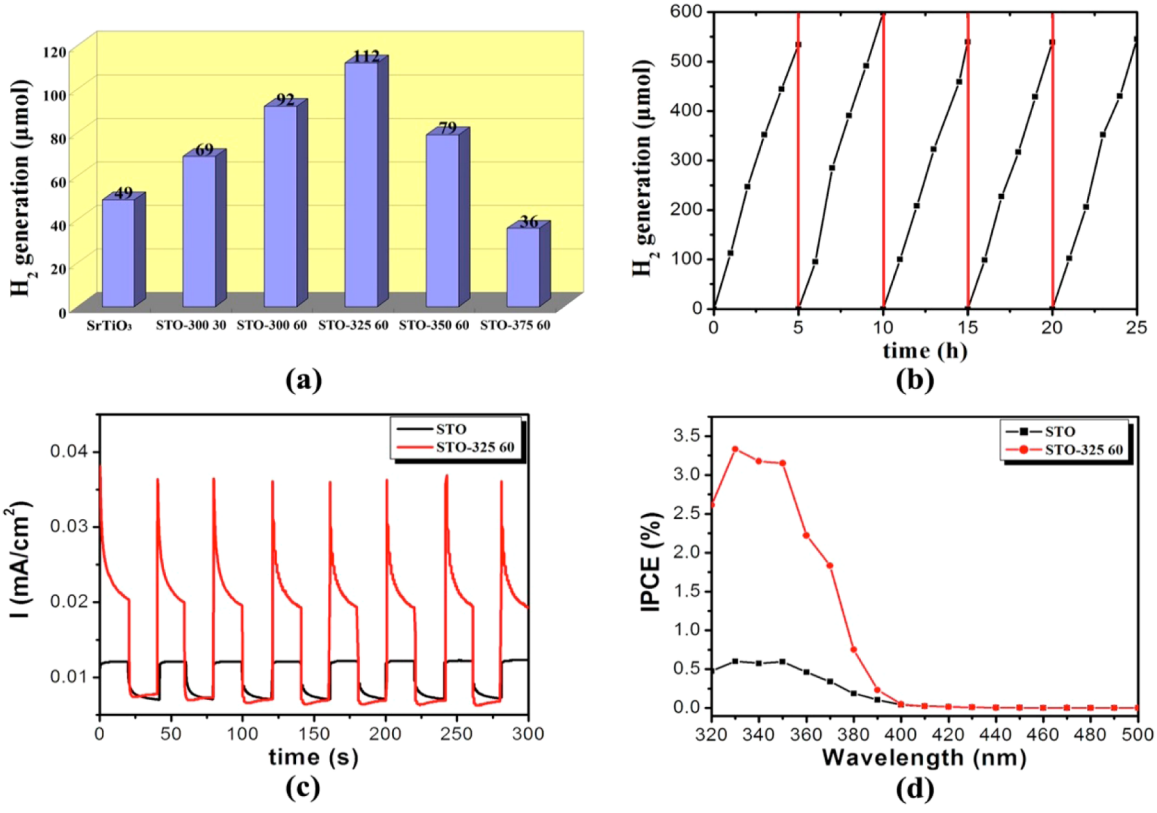

Figure 5. (a) Initial H_2 evolution rate of pristine $SrTiO_3$ and STO-*T t* samples; (b) Recycling measure of H_2 production through photocatalytic water splitting with STO-325 60, 50 mg photocatalyst with 1.0 wt % Pt loaded in 120 mL 25% aqueous methanol solution under UV−vis irradiations; (c) photocurrent response of pristine SrTiO3 and STO-325 60; (d) IPCE of the pristine $SrTiO_3$ and STO-325 60 collected at a bias voltage of −0.8 V versus Hg/Hg_2Cl_2.

dx.doi.org/10.1021/am5051907 | ACS Appl. Mater. Interfaces 2014, 6, 19184−19190

transient photocurrent response experiments of pristine $SrTiO_3$ and STO-325 60 were measured. As shown in Figure 5c, when the light was successively shuttled on and off, a series of photocurrent signals could be detected for $SrTiO_3$ and STO-325 60. However, the photoelectric current density of STO-325 60, 0.015 mA cm^{-2}, which was three times higher than that of pristine $SrTiO_3$ 0.005 mA cm^{-2}, implying that the charge separation in STO-325 60 has been enhanced remarkably by reducing the recombination of photogenerated charge carriers. In order to investigate the relationship between the light absorption of $SrTiO_3$ and its photocatalytic activity, IPCE (incident-photon-to-current conversion efficiency) measurements were performed on $SrTiO_3$ and STO-325 60 photoanodes at −0.8 eV (Figure 5d). In comparison with pristine $SrTiO_3$, the STO-325 60 exhibits greatly enhanced photocatalytic performance over the UV region. While in the visible light region, there is no observable improvement. It indicates that the enhanced photocatalytic activity of the STO-325 60 contributes from the improvement of charge separation of photogenerated charge carriers in the UV region.

CONCLUSION

In summary, a facile and general method has been introduced to fabricate oxygen vacancies on perovskite $SrTiO_3$ nanocrystals through a controllable solid-state reaction of $NaBH_4$ and crystalline $SrTiO_3$. STO samples with different oxygen vacancy concentrations on their surfaces, and photocatalytic activities have been prepared. A series of characterization and photocatalytic results indicate that oxygen vacancies on STO surfaces also play a key role in influencing the spectral absorption and photocatalytic performance of this perovskite metal oxide as simple oxides. More important, TGA measurement could be employed to determine the oxygen vacancy concentration. With the increase of oxygen defects on the STO surface, the light absorption of STO samples in visible and infrared regions has been enhanced remarkably, but this light adsorption plays a negligible effect on the expanse spectral response of photocatalytic. An optimum concentration of oxygen vacancies can improve the charge separation of photogenerated charge carriers, and thus provide a maximum enhancement of photocatalytic performance. However, an excess amount of oxygen vacancies results in a decrease of photocatalytic performance.

ASSOCIATED CONTENT

Supporting Information

More XPS, UV−vis spectra, XRD, and TGA-MS. This material is available free of charge via the Internet at http://pubs.acs.org.

AUTHOR INFORMATION

Corresponding Author

*E-mail: sunzc@ciomp.ac.cn.

Author Contributions

All authors have given approval to the final version of the manuscript.

Notes

The authors declare no competing financial interest.

ACKNOWLEDGMENTS

The authors thank the National Natural Science Foundation of China (No. 21301166, 21201159, 61361166004, and 61176016); Science and Technology Department of Jilin Province (No. 20130522127JH and 20121801) are gratefully acknowledged. Z.S. thanks the support of the "Hundred Talent Program" of CAS. Supported by open research fund program of State Key Laboratory of Luminescence and Applications (Changchun Institute of Optics, Fine Mechanics and Physics, CAS) and Key Laboratory of Functional Inorganic Material Chemistry (Heilongjiang University), Ministry of Education, P. R. China. HF acknowledges the support from the U.S. Department of Energy, Office of Basic Energy Sciences, Division of Materials Sciences and Engineering. Sandia is a multiprogram laboratory operated by Sandia Corporation, a wholly owned subsidiary of Lockheed Martin Corporation, for the U.S. Department of Energy's National Nuclear Security Administration under Contract DE-AC04-94AL85000.

REFERENCES

(1) Hoffmann, M. R.; Martin, S. T.; Choi, W.; Bahnemann, D. W. Environmental Applications of Semiconductor Photocatalysis. *Chem. Rev.* **1995**, *95* (1), 69−96.

(2) Chen, X.; Shen, S.; Guo, L.; Mao, S. S. Semiconductor-Based Photocatalytic Hydrogen Generation. *Chem. Rev.* **2010**, *110* (11), 6503−6570.

(3) Chen, C.; Ma, W.; Zhao, J. Semiconductor-Mediated Photodegradation of Pollutants under Visible-Light Irradiation. *Chem. Soc. Rev.* **2010**, *39* (11), 4206−4219.

(4) Kubacka, A.; Fernández-García, M.; Colón, G. Advanced Nanoarchitectures for Solar Photocatalytic Applications. *Chem. Rev.* **2011**, *112* (3), 1555−1614.

(5) Wen, F.; Li, C. Hybrid Artificial Photosynthetic Systems Comprising Semiconductors as Light Harvesters and Biomimetic Complexes as Molecular Cocatalysts. *Acc. Chem. Res.* **2013**, *46* (11), 2355−2364.

(6) Tong, H.; Ouyang, S.; Bi, Y.; Umezawa, N.; Oshikiri, M.; Ye, J. Nano-Photocatalytic Materials: Possibilities and Challenges. *Adv. Mater.* **2012**, *24* (2), 229−251.

(7) Kang, H. W.; Lim, S. N.; Park, S. B. Co-Doping Schemes to Enhance H_2 Evolution under Visible Light Irradiation over $SrTiO_3$:Ni/M (M = La or Ta) Prepared by Spray Pyrolysis. *Int. J. Hydrogen Energy* **2012**, *37* (7), 5540−5549.

(8) Ouyang, S.; Tong, H.; Umezawa, N.; Cao, J.; Li, P.; Bi, Y.; Zhang, Y.; Ye, J. Surface-Alkalinization-Induced Enhancement of Photocatalytic H_2 Evolution over $SrTiO_3$-Based Photocatalysts. *J. Am. Chem. Soc.* **2012**, *134* (4), 1974−1977.

(9) Jia, Y.; Shen, S.; Wang, D.; Wang, X.; Shi, J.; Zhang, F.; Han, H.; Li, C. Composite $Sr_2TiO_4/SrTiO_3$ (La, Cr) Heterojunction Based Photocatalyst for Hydrogen Production under Visible Light Irradiation. *J. Mater. Chem. A* **2013**, *1* (27), 7905−7912.

(10) Liu, P.; Nisar, J.; Pathak, B.; Ahuja, R. Hybrid Density Functional Study on $SrTiO_3$ for Visible Light Photocatalysis. *Int. J. Hydrogen Energy* **2012**, *37* (16), 11611−11617.

(11) Zou, F.; Jiang, Z.; Qin, X.; Zhao, Y.; Jiang, L.; Zhi, J.; Xiao, T.; Edwards, P. P. Template-Free Synthesis of Mesoporous N-Doped $SrTiO_3$ Perovskite with High Visible-Light-Driven Photocatalytic Activity. *Chem. Commun.* **2012**, *48* (68), 8514−8516.

(12) Kato, H.; Sasaki, Y.; Shirakura, N.; Kudo, A. Synthesis of Highly Active Rhodium-Doped $SrTiO_3$ Powders in Z-Scheme Systems for Visible-Light-Driven Photocatalytic Overall Water Splitting. *J. Mater. Chem. A* **2013**, *1* (39), 12327−12333.

(13) Yang, J.; Wang, D.; Han, H.; Li, C. Roles of Cocatalysts in Photocatalysis and Photoelectrocatalysis. *Acc. Chem. Res.* **2013**, *46* (8), 1900−1909.

(14) Wang, G.; Ling, Y.; Li, Y. Oxygen-Deficient Metal Oxide Nanostructures for Photoelectrochemical Water Oxidation and Other Applications. *Nanoscale* **2012**, *4* (21), 6682−6691.

(15) Lv, Y.; Zhu, Y.; Zhu, Y. Enhanced Photocatalytic Performance for the $BiPO_{4-x}$ Nanorod Induced by Surface Oxygen Vacancy. *J. Phys. Chem. C* **2013**, *117* (36), 18520−18528.

(16) Bai, X.; Wang, L.; Zong, R.; Lv, Y.; Sun, Y.; Zhu, Y. Performance Enhancement of ZnO Photocatalyst via Synergic Effect of Surface Oxygen Defect and Graphene Hybridization. *Langmuir* **2013**, *29* (9), 3097−3105.
(17) Chen, X.; Liu, L.; Yu, P. Y.; Mao, S. S. Increasing Solar Absorption for Photocatalysis with Black Hydrogenated Titanium Dioxide Nanocrystals. *Science* **2011**, *331* (6018), 746−750.
(18) Wang, Z.; Yang, C.; Lin, T.; Yin, H.; Chen, P.; Wan, D.; Xu, F.; Huang, F.; Lin, J.; Xie, X.; Jiang, M. Visible-Light Photocatalytic, Solar Thermal, and Photoelectrochemical Properties of Aluminium-Reduced Black Titania. *Energy Environ. Sci.* **2013**, *6* (10), 3007−3014.
(19) Zheng, Z.; Huang, B.; Lu, J.; Wang, Z.; Qin, X.; Zhang, X.; Dai, Y.; Whangbo, M.-H. Hydrogenated Titania: Synergy of Surface Modification and Morphology Improvement for Enhanced Photocatalytic Activity. *Chem. Commun.* **2012**, *48* (46), 5733−5735.
(20) Naldoni, A.; Allieta, M.; Santangelo, S.; Marelli, M.; Fabbri, F.; Cappelli, S.; Bianchi, C. L.; Psaro, R.; Dal Santo, V. Effect of Nature and Location of Defects on Bandgap Narrowing in Black TiO_2 Nanoparticles. *J. Am. Chem. Soc.* **2012**, *134* (18), 7600−7603.
(21) Zuo, F.; Wang, L.; Wu, T.; Zhang, Z.; Borchardt, D.; Feng, P. Self-Doped Ti^{3+} Enhanced Photocatalyst for Hydrogen Production under Visible Light. *J. Am. Chem. Soc.* **2010**, *132* (34), 11856−11857.
(22) Yu, X.; Kim, B.; Kim, Y. K. Highly Enhanced Photoactivity of Anatase TiO_2 Nanocrystals by Controlled Hydrogenation-Induced Surface Defects. *ACS Catal.* **2013**, *3* (11), 2479−2486.
(23) Tan, H.; Zhao, Z.; Niu, M.; Mao, C.; Cao, D.; Cheng, D.; Feng, P.; Sun, Z. A Facile and Versatile Method for Preparation of Colored TiO_2 with Enhanced Solar-Driven Photocatalytic Activity. *Nanoscale* **2014**, *6* (17), 10216−10223.
(24) Liu, G.; Han, J.; Zhou, X.; Huang, L.; Zhang, F.; Wang, X.; Ding, C.; Zheng, X.; Han, H.; Li, C. Enhancement of Visible-Light-Driven O_2 Evolution from Water Oxidation on WO_3 Treated with Hydrogen. *J. Catal.* **2013**, *307* (0), 148−152.
(25) Wang, J.; Wang, Z.; Huang, B.; Ma, Y.; Liu, Y.; Qin, X.; Zhang, X.; Dai, Y. Oxygen Vacancy Induced Band-Gap Narrowing and Enhanced Visible Light Photocatalytic Activity of ZnO. *ACS Appl. Mater. Interfaces* **2012**, *4* (8), 4024−4030.
(26) Lv, Y.; Yao, W.; Ma, X.; Pan, C.; Zong, R.; Zhu, Y. The Surface Oxygen Vacancy Induced Visible Activity and Enhanced UV Activity of a ZnO_{1-x} Photocatalyst. *Catal. Sci. Technol.* **2013**, *3* (12), 3136−3146.
(27) Ling, Y.; Wang, G.; Reddy, J.; Wang, C.; Zhang, J. Z.; Li, Y. The Influence of Oxygen Content on the Thermal Activation of Hematite Nanowires. *Angew. Chem., Int. Ed.* **2012**, *51* (17), 4074−4079.
(28) Grinberg, I.; West, D. V.; Torres, M.; Gou, G.; Stein, D. M.; Wu, L.; Chen, G.; Gallo, E. M.; Akbashev, A. R.; Davies, P. K.; Spanier, J. E.; Rappe, A. M. Perovskite Oxides for Visible-Light-Absorbing Ferroelectric and Photovoltaic Materials. *Nature* **2013**, *503* (7477), 509−512.
(29) Liu, G.; Yin, L.-C.; Wang, J.; Niu, P.; Zhen, C.; Xie, Y.; Cheng, H.-M. A Red Anatase TiO_2 Photocatalyst for Solar Energy Conversion. *Energy Environ. Sci.* **2012**, *5* (11), 9603−9610.
(30) Yu, H.; Zhao, Y.; Zhou, C.; Shang, L.; Peng, Y.; Cao, Y.; Wu, L.-Z.; Tung, C.-H.; Zhang, T. Carbon Quantum Dots/TiO_2 Composites for Efficient Photocatalytic Hydrogen Evolution. *J. Mater. Chem. A* **2014**, *2* (10), 3344−3351.
(31) Kang, Q.; Cao, J.; Zhang, Y.; Liu, L.; Xu, H.; Ye, J. Reduced TiO_2 Nanotube Arrays for Photoelectrochemical Water Splitting. *J. Mater. Chem. A* **2013**, *1* (18), 5766−5774.
(32) Feng, L.-L.; Zou, X.; Zhao, J.; Zhou, L.-J.; Wang, D.-J.; Zhang, X.; Li, G.-D. Nanoporous Sr-Rich Strontium Titanate: A Stable and Superior Photocatalyst for H_2 Evolution. *Chem. Commun.* **2013**, *49* (84), 9788−9790.
(33) Bai, H.; Juay, J.; Liu, Z.; Song, X.; Lee, S. S.; Sun, D. D. Hierarchical $SrTiO_3/TiO_2$ Nanofibers Heterostructures with High Efficiency in Photocatalytic H_2 Generation. *Appl. Catal. B: Environ.* **2012**, *125* (0), 367−374.
(34) Kimijima, T.; Kanie, K.; Nakaya, M.; Muramatsu, A. Solvothermal Synthesis of $SrTiO_3$ Nanoparticles Precisely Controlled in Surface Crystal Planes and Their Photocatalytic Activity. *Appl. Catal. B: Environ.* **2014**, *144* (0), 462−467.
(35) Sun, T.; Lu, M. Band-Structure Modulation of $SrTiO_3$ by Hydrogenationfor Enhanced Photoactivity. *Appl. Phys. A: Mater. Sci. Process.* **2012**, *108* (1), 171−175.
(36) Park, S.-M.; Ikegami, T.; Ebihara, K. Effects of Substrate Temperature on the Properties of Ga-Doped ZnO by Pulsed Laser Deposition. *Thin Solid Films* **2006**, *513* (1−2), 90−94.
(37) Chen, M.; Wang, X.; Yu, Y. H.; Pei, Z. L.; Bai, X. D.; Sun, C.; Huang, R. F.; Wen, L. S. X-ray Photoelectron Spectroscopy and Auger Electron Spectroscopy Studies of Al-Doped ZnO Films. *Appl. Surf. Sci.* **2000**, *158* (1−2), 134−140.
(38) Su, Y.; Lang, J.; Li, L.; Guan, K.; Du, C.; Peng, L.; Han, D.; Wang, X. Unexpected Catalytic Performance in Silent Tantalum Oxide through Nitridation and Defect Chemistry. *J. Am. Chem. Soc.* **2013**, *135* (31), 11433−11436.
(39) Janotti, A.; Varley, J. B.; Rinke, P.; Umezawa, N.; Kresse, G.; Van de Walle, C. G. Hybrid Functional Studies of the Oxygen Vacancy in TiO_2. *Phys. Rev. B* **2010**, *81* (8), 085212.
(40) Cronemeyer, D. C. Infrared Absorption of Reduced Rutile TiO_2 Single Crystals. *Phys. Rev.* **1959**, *113* (5), 1222−1226.
(41) Su, R.; Tiruvalam, R.; He, Q.; Dimitratos, N.; Kesavan, L.; Hammond, C.; Lopez-Sanchez, J. A.; Bechstein, R.; Kiely, C. J.; Hutchings, G. J.; Besenbacher, F. Promotion of Phenol Photodecomposition over TiO_2 Using Au, Pd, and Au−Pd Nanoparticles. *ACS Nano* **2012**, *6* (7), 6284−6292.